

Large amplitude electrostatic waves observed at a supercritical interplanetary shock

L.B. Wilson III,¹ C.A. Cattell,¹ P.J. Kellogg,¹ K. Goetz,¹ K. Kersten,¹ J.C. Kasper,² A. Szabo,³ M. Wilber⁴

Abstract. We present the first observations at an interplanetary shock of large amplitude (> 100 mV/m pk-pk) solitary waves and large amplitude (~ 30 mV/m pk-pk) waves exhibiting characteristics consistent with electron Bernstein waves. The Bernstein-like waves show enhanced power at integer and half-integer harmonics of the cyclotron frequency with a broadened power spectrum at higher frequencies, consistent with the electron cyclotron drift instability. The Bernstein-like waves are obliquely polarized with respect to the magnetic field but parallel to the shock normal direction. Strong particle heating is observed in both the electrons and ions. The observed heating and waveforms are likely due to instabilities driven by the free energy provided by reflected ions at this supercritical interplanetary shock. These results offer new insights into collisionless shock dissipation and wave-particle interactions in the solar wind. [Date: 08/13/2010]

1. Introduction

Collisionless shock waves are a topic of considerable interest in space and laboratory plasma physics due to their ability to efficiently heat and/or accelerate charged particles. Energy dissipation mechanisms in collisionless shocks have been the subject of study since the prediction of the existence of collisionless shocks [Kellogg, 1962]. Possible energy dissipation mechanisms include wave dispersion [Mellott and Greenstadt, 1984], particle reflection [Edmiston and Kennel, 1984; Kennel, 1987], macroscopic field effects [Bale and Mozer, 2007; Wygant et al., 1987], and anomalous resistivity due to wave-particle interactions [Gary, 1981]. Ion reflection is expected to occur when a shock has a Mach number that exceeds some theoretical critical Mach number (M_{cr}) above which the shock can no longer dissipate enough energy through resistive or dispersive effects to remain stable [Edmiston and Kennel, 1984; Kennel, 1987]. For realistic ranges of shock normal angle, θ_{Bn} , and plasma temperature, typical solar wind conditions will actually yield $M_{cr} \sim 1-2$ [Edmiston and Kennel, 1984; Kennel, 1987], suggesting particle reflection may occur even at low Mach number shocks. Greenstadt and Mellott [1987] examined ISEE 1 and 2 data for 100 quasi-perpendicular ($0.6 < M/M_{cr} < 4$) bow shock crossings to look for evidence of ion reflection in plasma wave measurements and found evidence to suggest ion reflection occurs even at subcritical collisionless shock waves. Other studies using ISEE 1 and 2 particle data report observations of reflected ions even for low Mach number ($M \sim 2$) quasi-perpendicular bow shock crossings [Sckopke et al., 1983].

The importance of wave-particle interactions in the total energy dissipation budget of collisionless shocks is not well known. Recent studies have found evidence to suggest that

wave-particle interactions may be more important than previously thought [Wilson III et al., 2007]. Some commonly expected instabilities and waves predicted to contribute to resistive energy dissipation in the transition region of quasi-perpendicular collisionless shocks are electrostatic (ES) ion-acoustic waves (IAWs), ES structures with Debye length scales with bipolar electric field signatures parallel to the background magnetic field, called solitary waves or electron phase space holes, modified two stream instability (MTSI), lower-hybrid-drift instability (LHDI), and electron cyclotron drift instability (ECDI) [Wu et al., 1984].

Wilson III et al. [2007] showed that the amplitude of ≥ 5 mV/m peak-to-peak IAWs increased with increasing Mach number and the shock strength. This is consistent with larger shock strengths causing larger cross-field currents, which may provide free energy for wave generation. The study also found that large amplitude IAWs had the highest probability of occurrence in the ramp region, consistent with theory [Gary, 1981]. Solitary waves have been observed at the terrestrial bow shock by Bale et al. [2002] and at IP shocks near 1 AU by Wilson III et al. [2007] and 8.7 AU by Williams et al. [2005]. Electron cyclotron harmonic, electron Bernstein, ($n + 1/2$), or "totem pole" waves have been observed throughout planetary magnetospheres [Barbosa et al., 1990; Matsumoto and Usui, 1997; Usui et al., 1999]. These emissions can be either broad or narrow in frequency range [Hubbard and Birmingham, 1978]. They are typically driven unstable by loss-cone or anisotropic electron distributions in the high energy hot electrons in planetary magnetospheres. Usui et al. [1999], in a study near the terrestrial magnetopause in the magnetosheath, found the emissions to be associated with increases in the ratio of hot (>100 eV) to cold (<100 eV) electron densities, n_h/n_c . To the best of our knowledge, these emissions have not been observed previously in the solar wind or at shocks.

Some previous studies of collisionless shocks have suggested that the electron heating can be adequately explained by the de Hoffmann-Teller potential or $\Delta\Phi^{dHT}$ [Scudder et al., 1986]. They argue that the associated normal quasi-static electric field explains the observed heating in the downstream electron distributions. In this scenario, wave-particle interactions in a shock ramp act only to cool and/or smooth the downstream distributions, filling voids of inaccessible regions in phase space. Exactly how the cross-shock potential arises and how it scales with upstream parameters are still poorly understood. The first measurements of the

¹Department of Physics and Astronomy, University of Minnesota, Minneapolis, Minnesota, USA.

²Harvard-Smithsonian Center for Astrophysics, Harvard University, Cambridge, Massachusetts, USA.

³NASA Goddard Space Flight Center, Greenbelt, Maryland, USA.

⁴University of California, Berkeley, Space Sciences Laboratory, Berkeley, California, USA.

quasi-static electric field in the shock ramp most likely under sampled the full electric field in the shock ramp [Wygant *et al.*, 1987], which is significant because the cross-shock potential arises from the accumulation of all the electric fields within a shock ramp not just the quasi-static electric fields [Bale and Mozer, 2007; Walker *et al.*, 2004; Wygant *et al.*, 1987]. Ignoring the high frequency electric fields may not be a valid assumption particularly when they reach large amplitudes due to their ability to trap and heat particles, a process distinctly different than the effects of the cross-shock potential [Dum *et al.*, 1974; Gary, 1981].

Simulations of high Mach number collisionless shock waves have found that electron phase space holes form in and around the ramp regions [Dyrud and Oppenheim, 2006; Matsukiyo and Scholer, 2006a]. These holes have a bipolar electric field signature parallel to the magnetic field if they propagate along the magnetic field. Due to their ability to efficiently exchange momentum between electrons and ions, the holes can heat and scatter particles. Simulations also show that the holes can couple with other wave modes like IAWs and lower hybrid waves, providing resistive dissipation [Dyrud and Oppenheim, 2006; Matsukiyo and Scholer, 2006a]. For over 30 years it has been theorized that IAWs nonlinearly interact with ions to form high energy tails and electrons to form flattop distributions [Dum *et al.*, 1974]. Bernstein-like emissions can interact with electrons through a cyclotron resonance causing perpendicular electron heating [Kumar and Tripathi, 2006].

Matsukiyo and Scholer [2006a] examined microinstabilities in the foot of supercritical collisionless shocks using a two dimensional PIC simulation with a realistic mass ratio ($M_i/m_e \sim 1836$). They observed six different types of instabilities excited in less than a gyroperiod of the reflected ions with the dominant modes including ECIDI, whistler instability, electron acoustic instability, and two different MT-SIs, MTSI-2 excited by relative drifts between incident electrons and reflected ions and MTSI-1 due to the relative drift between electrons and incident ions. Reflected ions cause the incident solar wind ions to decelerate in the shock foot, which locally decelerates the electrons to maintain current continuity in the shock normal direction. All these instabilities driven by the interaction of incident ions and electrons with reflected ions give rise to waves which scatter and heat the plasma, thus dissipating energy. The ECIDI, driven unstable by the interaction of the incident electrons and reflected ions, is predicted to resonantly interact with ions heating the bulk of the ion distribution and to preferentially heat electrons in the perpendicular direction [Forsslund *et al.*, 1970, 1972; Lampe *et al.*, 1972]. It should also be noted that Matsukiyo and Scholer [2006b] and Muschietti and Lembège [2006] observed the ECIDI in self-consistent one dimensional PIC simulations. To the best of our knowledge, the simulation performed by Matsukiyo and Scholer [2006a] is the only study of shock microinstabilities using a full two dimensional PIC code with realistic mass ratio.

This study is motivated by the examination of an unusual supercritical IP shock observed by the Wind spacecraft on 04/06/2000 [Wilson III *et al.*, 2009]. The previous study found unusual waveforms, called shocklets, upstream of the shock and strong electron heating across the shock ramp. We will focus on the unusually high electron heating observed in the ramp region. Strong perpendicular electron heating could be evidence of resistive heating due to wave-particle interactions [Thomsen *et al.*, 1985]. Within ± 5 seconds, corresponding to $\pm 14 c/\omega_{pi}$ (upstream ion inertial lengths where c is the speed of light and ω_{pi} is the average upstream ion plasma frequency) of the shock crossing, four waveform captures were obtained by the Wind spacecraft, two of which have frequency spectra consistent with the ECIDI and two with solitary wave signatures. The paper is organized as follows: in Section 2, we discuss the data sets and analysis techniques used in this study; in Section 3, we present our observations; in Section 4 we discuss our observations and compare to theory and simulations; and in Section 5, we make our conclusions.

2. Data Sets and Analysis

Waveform captures were obtained from the Wind/WAVES instrument [Bougeret *et al.*, 1995], through the time domain sampler (TDS) receiver, which provides a ~ 17 ms waveform capture of 2048 points (from here on, a waveform capture is called a TDS sample). TDS samples utilized herein provide two components of the electric field in the XY-GSE plane, called E_x and E_y . The spin axis (roughly the Z-GSE component) electric field was not sampled for these TDS samples. The TDS buffer stores and evaluates waveforms based upon their amplitude. Thus if small amplitude waves are observed, they will not be stored and transmitted to the ground if larger amplitude waves fill the buffer. We define $|E_{xy}| = \sqrt{E_x^2 + E_y^2}$ as the maximum peak-to-peak (pk-pk) amplitude of the TDS samples. We only measure two components of the electric field vector, roughly in the XY-GSE plane. This limits our ability to measure electric fields parallel(perpendicular) to the magnetic field direction. Thus, when rotating the electric field components into magnetic field-aligned coordinates (FACs), we rotate the fields by the angle between the positive X-antenna and the XY-GSE projection of the magnetic field vector. In FACs, we define the subscript $\parallel(\perp)$ as the direction parallel(perpendicular) to the XY-GSE projection of the magnetic field direction. However, if a significant fraction of the magnetic field is in the Z-GSE direction, the measured E_{\parallel} may be significantly different from the total electric field along the magnetic field. The converse applies to the measured values of E_{\perp} . The lack of full 3D electric field measurements can influence the determination of polarization as well.

To analyze the waveforms dynamically in time and frequency, we computed the Morlet wavelet transform [Torrence and Compo, 1998a] for the four waveforms examined in this study. The wavelet transform has a number of distinct advantages over windowed FFTs, but the two most important for our analysis are the resolved dynamic power spectra at low frequencies (~ 200 to 1000 Hz) and the analysis of non-stationary power intensifications at many different frequencies simultaneously [Torrence and Compo, 1998b]. Windowed FFTs have imposed periodicity and have a single time scale while wavelets do not. However, two sanity checks are performed to expose noise or numerical artifacts due to the interpolation routines. The cone of influence is a calculation done to determine the time-frequency region of the wavelet transform which is subject to edge effects. Thus, values above (with respect to frequency and time) this line can be trusted to not have artificial effects due to the finite time range of the data. The second calculation determined the 95% confidence level (also called "significant at the 5% level"). The 95% confidence level outlines regions of the wavelet transform which enclose intensities above 95% of the data. The 95% confidence level can be calculated from a theoretical red or white noise spectrum, but here we used the actual waves since they are clearly well above the background noise level of the solar wind ($\lesssim 0.1$ mV/m at 1 AU). Both significance tests are used to increase our ability to make quantitative analysis using the wavelet transforms.

The magnetic field instrument on board Wind [Lepping *et al.*, 1995] is composed of dual triaxial fluxgate magnetometers. High time resolution (HTR) magnetic field data, sampled at ~ 11 samples/s, were used to define the ramp region, or transition region, of the IP shock, as well as to identify low frequency magnetic fluctuations upstream of the ramp [Wilson III *et al.*, 2009]. The ramp is defined as the

interval from the point of lowest magnetic field immediately preceding the discontinuity (in magnetic field amplitude) to the point of highest magnetic field immediately following the discontinuity [Farris *et al.*, 1993].

Low energy (<30 keV) electron and ion distributions were obtained from the Wind/3DP EESA and PESA particle detectors [Lin *et al.*, 1995]. The EESA Low (EL and ELB in burst mode) instrument can measure electrons at 15 different energies from a few eV to a little more than a keV. The PESA Low (PL and PLB in burst mode) instrument measures ions at 14 different energies from as low as 100 eV to as high as 10 keV (typical range in the solar wind is 700 eV to 6 keV). The instrument is used primarily for bulk solar wind properties like ion velocity, density, and temperature. The PESA High (PH and PHB in burst mode) instrument measures ions at 15 different energies from as low as 80 eV to as high as 30 keV (typical range in the solar wind is 500 eV to 28 keV). The time resolution of each instrument depends on whether the instruments are in burst mode or not. In burst mode, both EESA and PESA instruments return full three dimensional particle distributions every three seconds (~ 1 spin period). Electron and ion distributions were examined for possible wave free energy sources and evidence of heating. Estimates of the electron temperature anisotropies in both the cold dense core (subscript c) and the hotter more tenuous halo (subscript h) can be obtained from full 3D electron distributions. The method for determining the break energy between halo and core electrons is outlined by [Wilson III *et al.*, 2009].

High energy (>30 keV) electron and proton measurements were obtained from three pairs of double-ended solid state telescopes (SSTs), each with a pair or triplet of closely stacked silicon semiconductor detectors [Lin *et al.*, 1995]. The SSTs provide a full 4π steradian coverage with a $22.5^\circ \times 36^\circ$ angular resolution and $\Delta E/E \approx 0.2$ energy resolution. One side of each detector is covered in a thin lexan foil (SST Foil) to stop protons up to ~ 400 keV while leaving electrons relatively unaffected. The opposite end of the detector is left open (SST Open) using a common broom magnet to sweep away electrons below ~ 400 keV while leaving the protons relatively unaffected. Thus, in the absence of any higher energy (penetrating) particles, the SST Foil counts only electrons and the SST Open counts only ions.

The relevant shock parameters, determined by Kasper [2007], are the shock normal angle, θ_{Bn} , fast mode Mach number, M_f , shock normal vector, \hat{n} , upstream normal flow velocity in the shock frame, U_n , upstream solar wind velocity, \mathbf{V}_{sw} , and shock strength, N_{i2}/N_{i1} . The values for the 04/06/2000 event are: $M_f \sim 4$, $\theta_{Bn} \sim 68^\circ$, $U_n \sim 278$ km/s, $\mathbf{V}_{sw} \sim \langle -370., -18., -22. \rangle$ km/s (GSE coordinates), $\hat{n} \sim \langle -0.98, -0.08, -0.16 \rangle$ (GSE coordinates), and $N_{i2}/N_{i1} \sim 4$.

3. Observations

Figure 1 shows a plot of the magnitude (first panel) and the GSE components of the magnetic field (labeled with color coded component letters, second panel) for the 04/06/2000 event between 16:32:03 and 16:32:15 UT. The shock arrival time, or middle of the magnetic ramp, is 16:32:09.2 UT. The shaded regions correspond to the time ranges of each particle distribution found in Figure 2. The vertical color-coded lines labeled with capital letters indicate the locations of the TDS samples shown in Figure 3.

Figure 2 shows four ion (top row) and electron (bottom row) distribution functions plotted with the horizontal axes corresponding to the direction parallel to the magnetic field. The plots are projected into the plane produced by the solar wind velocity and the local magnetic field. The electron

and ion velocity ranges in the plots are $\pm 20,000$ km/s and $\pm 2,500$ km/s, respectively. The phase space density color scales for each instrument are the same for the four different distributions in each row.

A summary of the relative changes in moments for the four electron distributions shown in Figure 2 can be found in Table 1. The relative change in any given moment is defined as $\Delta Q_s = ((Q_f - Q_i)/Q_i)_s \times 100\%$, where the subscripts f and i represent the final and initial state, respectively and the subscript s represents the particle species (*e.g.* core). The final and initial state for the calculations in Table 1 are specific only to the four distributions shown in Figure 2. Thus, the final state refers to the distribution starting at 16:32:12 UT and the initial state refers to the distribution starting at 16:32:03 UT. The top half of the table shows the values for ΔT_{es} , $\Delta T_{\perp s}$, $\Delta T_{\parallel s}$, and $\Delta(T_{\perp}/T_{\parallel})_s$ for the core, halo, and entire distribution (*i.e.* core and halo combined). The bottom of Table 1 shows the global changes (downstream, subscript 2, over upstream, subscript 1) across the 04/06/2000 event for the core, halo, and entire distribution. Here, the subscripts 1 and 2 refer to asymptotic values for the upstream and downstream estimated by averaging the quantities over 10 minute intervals in each region (*i.e.* outside of the time period shown in Figure 1 and calculated for more than just the four distributions shown herein). The quantities for global changes shown in Table 1 are the average, perpendicular, and parallel temperatures.

The core electrons show the strongest heating in bulk, parallel, and perpendicular, components while the halo dominates in the change in temperature anisotropy. Note also that there appears to be a preference toward perpendicular heating as indicated by $\Delta T_{\perp s}$ for all three electron components. The middle part of Table 1 shows the specific values of $(T_{\perp}/T_{\parallel})_s$ for the core, halo, and entire energy range for each distribution shown in Figure 2. Notice that all three temperature anisotropies increase across the shock ramp, with the core increasing by $\gtrsim 30\%$ and the halo by $\gtrsim 58\%$. The global changes across the shock show a preference for perpendicular heating as well, increasing by almost a factor of four (see bottom of Table 1).

To be more quantitative, let us define the following parameter, α , used by Omid *and Winske* [1990] as a test of whether or not the shock is heating the particles adiabatically:

$$\alpha \equiv \left(\frac{T_{es,2}}{T_{es,1}} \right) - \left(\frac{N_2}{N_1} \right)^{\gamma-1} \quad (1a)$$

$$\alpha_{\perp} \equiv \left(\frac{T_{es,2\perp}}{T_{es,1\perp}} \right) - \left(\frac{N_2}{N_1} \right)^{\gamma-1} \quad (1b)$$

where $T_{es,j}$ is the asymptotic estimate of the electron temperature in for the regions defined by the subscript, j , which represents the upstream ($j = 1$) and downstream ($j = 2$), $T_{es,j\perp}$ are the perpendicular asymptotic estimates of the electron temperature, N_j are the asymptotic estimates of the particle density, and γ is the ratio of specific heats (here we used 5/3). If the factor α is equal to zero, then the electrons were heated adiabatically. If the $\alpha > (<) 0$, then the electrons were over(under) heated across the shock. All the asymptotic values of interest are given in Table 2 for comparison with the same definition for the ΔQ quantities as in Table 1. As one can see, the only shock with positive values of α for the entire electron distribution is the 2000-04-06 event. Oddly enough, the two weakest events, 1996-04-03 and 1996-04-08, have $\alpha > 0$ for both the core and halo electrons but $\alpha < 0$ when the entire distribution is considered. Although the values of ΔB and $\Delta T_{\perp,e}$ for the 2000-04-06 event are roughly the same, this result is unique to this event.

The differences in electron heating between the 04/06/2000 event and the four more-typical events are: 1) a global decrease in $T_{h,\parallel}$ across the shock, 2) an increase by over a

factor of three in T_{ce} and T_e across the shock, 3) a global increase in both $T_{c,\perp}/T_{c,\parallel}$ and $T_{h,\perp}/T_{h,\parallel}$ across the shock, 4) a global decrease in both $T_{h,\parallel}/T_{c,\parallel}$ and $T_{h,\perp}/T_{c,\perp}$ across the shock, and 5) sustained flattop electron distributions downstream for over an hour. We suggest that these differences are the result of wave-particle heating.

Figure 3 shows four TDS samples plotted in FACs at the times shown by the vertical lines in Figure 1. For each TDS sample, the magnetic field estimates were determined by averaging the HTR MFI data over the time range of the TDS sample. The angle of the magnetic field unit vector out of the XY-GSE plane, θ_{Bxy} , for each TDS sample is: $+10^\circ$ for **A**, $+10^\circ$ for **B**, -10° for **C**, and -31° for **D**. The relative scales for both E_{\parallel} (shown in red) and E_{\perp} (shown in blue) are shown with the vertical arrows in each plot (*e.g.* wave **D** is ~ 160 mV/m pk-pk for E_{\perp}). The peak values of $|E_{xy}|$ for the four TDS samples are ~ 39 , ~ 35 , ~ 20 , and ~ 166 mV/m. Note that these values of $|E_{xy}|$ are a lower bound to the actual maximum amplitudes of the waves since, as discussed in Section 2, we only measure two components of the electric field. Below the four waveforms are their associated hodograms. The time ranges of the hodograms are defined by the magenta boxes overlaying the waveforms. The solid green line corresponds to the XY-GSE projection of the shock normal vector, $\mathbf{n}_{xy}/|\mathbf{n}|$, which was roughly 10° out of the plane of measurement for each TDS sample. The projection of the shock normal vector was scaled to the maximum value of $|E_{xy}|$ for each TDS sample for ease of comparison to the polarization of the electric fields.

Each panel in Figure 4 represents a Morlet wavelet transform power spectral density plot of a single component of a waveform from Figure 3, E_{\parallel} on the left and E_{\perp} on the right. In each panel, two horizontal lines, a bowl shaped line, and multiple contours are plotted. The two horizontal lines correspond to the fundamental and first harmonic of the electron cyclotron frequency. The cyclotron frequency and first harmonic were calculated by interpolating the magnitude of the magnetic field over the duration of each TDS sample. The bowl-like line corresponds to the cone of influence and the contours correspond to the 95% confidence level. The top three rows share the same power range of 0.01 to 1000 (mV/m)²/Hz for the wavelets, while waveform **D** ranged from 0.05 to 45000 (mV/m)²/Hz because of its much larger amplitude.

Further examination of the wavelet transforms of waveforms **A** through **D** show enhanced power near the fundamental and first harmonic of the electron cyclotron frequency (f_{ce}) for E_{\perp} and E_{\parallel} . Half-integer harmonic power intensifications are most easily seen in the E_{\parallel} component of waveform **B**, outlined by the black box in Figure 4. However, the large amplitude of the higher frequency components makes a detailed analysis difficult for these events. Figures 5 through 8 present examples of snapshots of windowed FFTs for the four waveforms from Figure 3 to provide a complementary way to examine the power spectra. The left-hand column of panels shows E_{\parallel} , the power spectra (mV/m²/Hz) versus frequency (kHz) for the orange box, and the power spectra versus frequency for the black box, respectively. The right-hand column shows the same for E_{\perp} . The vertical lines in the power spectra correspond to integer (green) and half-integer (purple) multiples of the electron cyclotron frequency. All power spectra plots in Figures 5 and 6 range from 10^{-5} to 4×10^{-1} while in Figures 7 and 8 they range from 10^{-6} to 2×10^0 .

Figures 5 through 8 show that waveforms **A** through **D** have mixtures of integer half-integer multiples of the electron cyclotron frequency, f_{ce} , that change throughout the TDS samples. Note that the maximum Doppler shifted IAW frequency for waveform **A**(**B**) was estimated to be roughly 7.5 kHz(8.5 kHz), assuming wavelengths consistent with the measurements of *Fuselier and Gurnett* [1984], and the background noise level for this event is roughly 10^{-6} mV/m²/Hz.

The images clearly illustrates how the waveforms shift power between integer and half-integer harmonics of f_{ce} during the duration of the TDS samples. If we calculate the power spectrum using the entire time range for each TDS sample, the shifting peaks smear together into one peak. Thus, the combination of wavelet and windowed FFT analysis shows that waveforms **A** through **D** exhibit mixtures of integer and half-integer multiples of f_{ce} throughout the samples. Waveforms **C** and **D** differ from waveforms **A** and **B** in that they do not show broad power enhancements above 4 kHz. The difference is likely due to the fact that waveforms **A** and **B** are composed of IAWs and cyclotron harmonic waves whereas the power spectra for waveforms **C** and **D** are dominated primarily by the solitary waves. Also, waveforms **A** and **B** often have $E_{\perp} > E_{\parallel}$, consistent with cyclotron harmonic or Bernstein-like waves [*Usui et al.*, 1999]. Note that $1/f_{ce} \sim 1.95$ ms(1.62 ms) for waveform **C**(**D**). Also, the solitary wave in waveform **C** near 4 ms(8 ms) has a period of ~ 1.33 ms(1.44 ms), slightly smaller than the cyclotron period. The solitary wave in waveform **D** near 5 ms(8 ms) has a period of ~ 1.56 ms(1.67 ms), almost identical to the cyclotron period. Thus, the Bernstein-like emissions are still simultaneously observed with the solitary waves up to $\sim 14 c/\omega_{pi}$ away from the shock ramp. These integer and/or half-integer harmonic intensifications are consistent with previous observations of cyclotron harmonic or Bernstein-like waves [*Usui et al.*, 1999].

Figure 9 shows the 2D Hammer-Aitoff projection of 27 and 40 keV electrons from the SST Foil instrument on Wind between 16:31:01 UT and 16:32:15 UT. The Hammer-Aitoff projections display a full 4π steradian of the measured particles. The data are plotted in units of phase-space density (s³cm⁻³km⁻³) with ranges of 5×10^{-22} (purple) to 2.2×10^{-21} (red) for the 27 keV electrons and 5×10^{-22} (purple) to 1.1×10^{-21} (red) for the 40 keV electrons. Different scales were used for the two energies to highlight the intensification near the center of each plot. The SST Foil distributions are sampled every 12-13 seconds (~ 4 spin periods) for this event. Four symbols are projected onto the 3D maps corresponding to relevant vectors including: +, the magnetic field direction, \diamond , the anti-parallel magnetic field direction, *, the solar wind velocity direction (roughly negative X-GSE for this event), and Δ , the shock normal vector. The dotted lines denote 30° increments in both latitude and longitude. The beam-like feature, observed in every SST distribution of Figure 9, parallel to the magnetic field is also intermittently observed for nearly 20 minutes upstream of the shock ramp (not shown). It is not clear whether the beam-like feature is a contributing source of free energy for the solitary waves, but electron beams have been associated with solitary wave observations in many studies (*e.g.* *Ergun et al.* [1998a]). Also, a beam-like feature roughly 30° to the right of the shock normal and solar wind direction is observed in both energies with strong enhancements in the last two panels. Correspondingly, there is another beam-like enhancement roughly 180° to the right of the beam-like feature near the shock normal and solar wind directions, suggesting they are contaminated data bins.

4. Discussion

Because the full three dimensional electric field is not measured, we can infer some properties of the waves but cannot definitively determine the polarization. Recall that θ_{Bxy} is not zero for any of the four waveforms. If we assume the solitary waves propagate along the magnetic field, the relative magnitude of E_{\perp} to E_{\parallel} should be smaller for waveform **D** than **C**. Based on the usual model of phase space holes, we expect to observe a unipolar E_{\perp} and bipolar E_{\parallel}

except in the singular case that the spacecraft passes exactly through the center of the hole. The most likely explanation for the observation of a bipolar E_{\perp} is the result of not measuring E_z . Thus, the smaller bipolar E_{\perp} to E_{\parallel} in waveform **D** compared to **C** is likely due to the larger θ_{Bxy} .

Typical TDS samples in most IP shock ramps are consistent with Doppler shifted IAWs [Wilson III et al., 2007]. For comparison to waveforms **A** and **B**, Figure 10 shows an example of a typical IAW observed in the 04/08/1996 IP shock ramp, one of the four lower Mach number shocks examined by Wilson III et al. [2009]. The parallel(perpendicular) components are plotted in red(blue) with the associated hodogram to the right. The hodogram has the XY-GSE projection of the shock normal vector plotted as a solid green line, as in the hodograms of Figure 3. The wavelet transforms for the parallel and perpendicular components are plotted below the waveform captures. The IAW wavelet shows a strong isolated band of power between ~ 2 -5 kHz for both components. This isolated, relatively narrow, band of emission is typical of the IAWs observed at the four lower Mach number IP shocks. We also examined snapshot FFTs of the IAWs in the four more-typical IP shock ramps and found that the waves show slight enhancements below ~ 1 kHz, but no noticeable enhancements near integer and half-integer harmonics were observed.

The wavelets for waveforms **A** through **D** are clearly different from the wavelet in Figure 10, supporting our argument that these waveforms are not simple IAWs, but rather are most likely to be a mixture of multiple modes. Thus, we argue that waveforms **A** and **B** are not simple IAWs for the following reasons: 1) neither waveform electric field component oscillates symmetrically about zero; 2) both waveforms have mixtures of frequencies consistent with IAWs and electron cyclotron harmonics in their power spectra; and 3) the polarizations are correlated with the shock normal vector, not the magnetic field. Note that the waves observed by Hull et al. [2006] are similar to waveforms **A** and **B**, but we feel Hull et al. [2006] misattributed them to simple IAWs.

Further evidence to suggest that our observations are consistent with the EC DI is shown using a simple test of linear instability. Using the EC DI instability criterion, at the Debye length cutoff or $(k \lambda_{De}) > 1$, determined from Equation 15 in Forsslund et al. [1972] under the observed conditions, we found that the EC DI instability criterion estimates are a factor of 20 or more above the threshold. Therefore, we argue that the instability criterion determined by Forsslund et al. [1972] is easily satisfied.

To further examine the consistence of the observed waves with the EC DI, we looked at ion measurements from 10's of eV to a few MeV, using the PH and SST Open detectors, for reflected ion signatures, the source of free energy for the EC DI. No beam-like or gyrophase-restricted features could be definitively discerned in high energy ion SST Open measurements near the shock ramp. The SST measurements did show enhancements in the energy flux of 1-6.7 MeV ions and 100-500 keV electrons (not shown herein) upstream of the 04/06/2000 event concurrent with the 12 shocklets observed by Wilson III et al. [2009]. However, simultaneous increases in high energy particle fluxes in and around low frequency waves is not unusual [Sanderson et al., 1985]. We also examined distributions from the PH instrument (shown in Figure 2). We did not detect reflected ion beams using the PH detector due to the combination of two factors: 1) the 2000-04-06 event had very atypical ion distributions upstream called diffuse ions, thought to be remnants of reflected ion beams scattered by wave-particle interactions, [Paschmann et al., 1981] and 2) UV-light contamination. Note 12 shocklets of the type observed upstream of this event have been shown to have a one-to-one correlation with reflected ions observed as diffuse ion distributions [Hoppe et al., 1981, 1982; Hoppe and Russell, 1983], as observed in this case as well. Thus, the

simultaneous observation of shocklets with diffuse ions is evidence that reflected ions exist upstream of the 04/06/2000 IP shock. A cursory comparison of the shock parameters for this event with the critical Mach number estimates of Edmiston and Kennel [1984] suggest that it is almost certainly supercritical, which would also entail ion reflection [Greenstadt and Mellott, 1987]. Since the percentage of reflected ions relative to incident increases with increasing Mach number [Kennel et al., 1985], the 2000-04-06 event likely reflects more ions than the four more-typical events. It is possible, therefore, that the 2000-04-06 event surpassed a threshold for the minimum percentage of reflected ions relative to incident ions necessary for the EC DI to become unstable. We also observe a beam-like feature seen in the high energy electrons; although it likely has a very low density compared to the background density, it may contribute to the free energy needed to drive the observed waveforms. Note that we observe this beam-like feature for over 20 minutes upstream modulated in intensity concurrently with shocklets.

The 04/06/2000 event was the only shock of the five studied in detail to show strong sustained core ion heating across the shock. Although the PL detector has a narrow field of view ($\sim 180^{\circ} \times 14^{\circ}$) compared to PH ($\sim 360^{\circ} \times 14^{\circ}$), which could limit the accurate measurement of the solar wind in the immediate downstream region of strong shocks. We determined the relative accuracy of the PL measurements by comparing the downstream density measured by the PL detector to the downstream density estimated from the plasma line (indicative of local density) seen by the WAVES thermal noise receiver [Bougeret et al., 1995]. We only use the temperature increase determined from the PL detector as a qualitative proxy for the bulk ion temperature increase. The sustained ion temperature increase, measured with PL, across the 04/06/2000 shock was roughly a factor of 7 for $T_{i,\perp}$ and 5 for $T_{i,\parallel}$ with spikes in downstream temperatures exceeding factors of 8 and 6 respectively, consistent with previous observations [Thomsen et al., 1985]. However, the the four more-typical events showed ion temperature increases that were less than a factor of three. The PH distributions showed qualitatively similar changes.

Some of the ion heating may be due to the large amplitude solitary waves (electron phase space holes), which act like clumps of positive charge scattering and heating ions. Observations have shown that the change in perpendicular ion temperature across a train of electron holes can be comparable to the initial ion thermal energy [Ergun et al., 1998b]. The solitary waves may also be contributing to the observed changes in the electron distributions across the shock since their positive potentials can trap incident electrons [Dyrud and Oppenheim, 2006; Lu et al., 2008]. Solitary waves can either couple to or directly cause the growth of IAWs [Dyrud and Oppenheim, 2006], whistler mode waves [Lu et al., 2008], and/or electron acoustic waves [Matsukiyo and Scholer, 2006a]. Thus, solitary waves can directly heat/scatter particles or indirectly heat/scatter particles through the generation of or coupling to secondary waves.

A distinct difference in both electron and ion properties is observed across the 04/06/2000 shock compared to the other four events of Wilson III et al. [2009]. The ions show strong heating in both the bulk of the ion distribution and high energy tail (observed as diffuse ions for the 04/06/2000 event), while all four more-typical events only showed evidence for slight heating in the high energy ion tails. The 04/06/2000 event is also the only event to show sustained (over an hour) electron heating downstream of the shock ramp observed as flattop distributions, while the four more-typical events showed weak heating consistent with adiabatic compression. The core and halo electron heating is strongly anisotropic ($T_{\perp} > T_{\parallel}$) in the 04/06/2000 event,

while the electron heating in the four more-typical events showed no particular preference towards parallel or perpendicular, consistent with previous studies of marginally critical shocks [Thomsen *et al.*, 1985]. Typical supercritical quasi-perpendicular shocks exhibit perpendicular heating due to adiabatic compression and parallel heating due to a two-step process whereby the cross-shock potential accelerates the electrons parallel to the magnetic field and then the free energy associated with this accelerated beam excites microinstabilities, which redistribute the electrons in phase space to form flattop distributions [Thomsen *et al.*, 1987]. This two-step process leads to a roughly isotropic electron distribution in the downstream region of typical supercritical quasi-perpendicular shocks. The isotropy increases as one moves further into the downstream region, consistent with relaxation of the distributions due redistribution in phase space [Thomsen *et al.*, 1985, 1987]. The core electrons in the 04/06/2000 event, however, are observed to become more anisotropic ($T_{c,\perp}/T_{c,\parallel}$ increases) as one progresses further downstream for up to an hour after the shock encounter (not shown). Adiabatic compression due to the conservation of the first adiabatic invariant cannot explain this observation since the magnetic field magnitude does not correlate with $T_{c,\perp}$ in the downstream, as shown quantitatively in Table 2. These observations suggest that wave heating is important.

An examination of electron distributions at other supercritical shocks (not shown) showed particle heating resulting in parallel flattop and perpendicular heated Maxwellians. The heating was predominantly in the parallel direction immediately downstream of the shock but isotropized as one progressed further into the downstream, in agreement with previous observations [Feldman *et al.*, 1983; Thomsen *et al.*, 1987]. In contrast, the 04/06/2000 event showed perpendicular heating dominating in the downstream and $T_{c,\perp}/T_{c,\parallel}$ increasing as one progressed farther downstream, suggesting wave heating is important.

Strong quasi-static electric fields have been observed at collisionless shocks [Wygant *et al.*, 1987; Walker *et al.*, 2004; Bale and Mozer, 2007] and used to help explain particle heating [Scudder *et al.*, 1986; Thomsen *et al.*, 1987]. Particle heating due to the cross-shock potential through a two step process of acceleration and relaxation is expected to create stronger parallel heating of the core electrons [Thomsen *et al.*, 1987], not perpendicular as is seen here.

The above discussions indicate that the waves are consistent with the ECDI because: 1) the polarizations are primarily aligned with the shock normal direction, not the magnetic field direction; 2) the frequency spectrum shows integer and half-integer cyclotron harmonics; 3) the broad power intensifications at frequencies above 1 kHz of waveforms **A** and **B** are inconsistent with typical IAWs; and 4) we observed strong and preferentially perpendicular electron heating that is consistent with cyclotron heating as described in Forslund *et al.* [1972] and Matsukiyo and Scholer [2006a].

5. Conclusions

We present the first observations of large amplitude (>100 mV/m pk-pk) solitary waves and large amplitude (~ 30 mV/m pk-pk) waves exhibiting characteristics consistent with electron Bernstein waves at an interplanetary shock. Waveforms **A** through **D** in Figures 5 through 8 all clearly show enhanced power near integer and half-integer harmonics of the cyclotron frequency. Waveforms **A** and **B** show significant power along the shock normal and are obliquely polarized with respect to the magnetic field, consistent with the ECDI. Strong particle heating in both the

halo and core of the electrons and ions is observed near these waves, consistent with the simulation results of Matsukiyo and Scholer [2006a].

Waves with power spectra exhibiting characteristics of both IAWs and Bernstein-like emissions are consistent with the predicted spectrum of the ECDI. The IAWs are Doppler shifted and resonantly interact with the Bernstein-like emissions, coupling to form a time-dependent diffuse frequency and wave vector spectrum [Matsukiyo and Scholer, 2006a]. The ECDI is an attractive candidate for the event herein because it can explain both the particle heating and the atypical waveforms. The current produced by the relative drift between incident electrons and reflected ions is unstable to the ECDI. Our observations suggest that this current is the source of free energy for the waveforms observed in the 2000-04-06 event.

This is the first study to report on the simultaneous observation of electron beams with large amplitude Bernstein-like waves and solitary waves at an IP shock. The preference for perpendicular ion heating is consistent with previous bow shock observations [Thomsen *et al.*, 1985], but the perpendicular electron heating is not. The polarizations and frequencies of the wave modes observed are inconsistent with previous observations of waves at IP shocks [Wilson III *et al.*, 2007, 2009]. These results suggest a need for further investigation into the detailed microphysics of collisionless shock dissipation, particularly for higher Mach number events. Future studies will examine other IP shocks with similar shock parameters, looking for signatures of ion reflection and wave modes of the type presented herein.

Acknowledgments. We thank R. Lin (3DP), K. Ogilvie (SWE), and R. Lepping (MFI) for the use of data from their instruments. We would also like to thank M. Pulupa, S.D. Bale, and P. Schroeder for technical help with the 3DP software and analysis. We thank Linghua Wang for help in calibration of the SST Foil data. This research was supported by NESSF grant NNX07AU72H and grant NNX07AI05G.

References

- Bale, S. D., and F. S. Mozer (2007), Measurement of Large Parallel and Perpendicular Electric Fields on Electron Spatial Scales in the Terrestrial Bow Shock, *Phys. Rev. Lett.*, *98*, 205,001–+, doi:10.1103/PhysRevLett.98.205001.
- Bale, S. D., A. Hull, D. E. Larson, R. P. Lin, L. Muschietti, P. J. Kellogg, K. Goetz, and S. J. Monson (2002), Electrostatic Turbulence and Debye-Scale Structures Associated with Electron Thermalization at Collisionless Shocks, *Astrophys. J.*, *575*, L25–L28, doi:10.1086/342609.
- Barbosa, D. D., W. S. Kurth, I. H. Cairns, D. A. Gurnett, and R. L. Poynter (1990), Electrostatic electron and ion cyclotron harmonic waves in Neptune’s magnetosphere, *Geophys. Res. Lett.*, *17*, 1657–1660, doi:10.1029/GL017i010p01657.
- Bougeret, J.-L., et al. (1995), Waves: The Radio and Plasma Wave Investigation on the Wind Spacecraft, *Space Science Reviews*, *71*, 231–263, doi:10.1007/BF00751331.
- Dum, C. T., R. Chodura, and D. Biskamp (1974), Turbulent Heating and Quenching of the Ion Sound Instability, *Phys. Rev. Lett.*, *32*, 1231–1234, doi:10.1103/PhysRevLett.32.1231.
- Dyrud, L. P., and M. M. Oppenheim (2006), Electron holes, ion waves, and anomalous resistivity in space plasmas, *J. Geophys. Res.*, *111*, 1302–+, doi:10.1029/2004JA010482.
- Edmiston, J. P., and C. F. Kennel (1984), A parametric survey of the first critical Mach number for a fast MHD shock., *J. Plasma Physics*, *32*, 429–441.
- Ergun, R. E., et al. (1998a), FAST satellite observations of large-amplitude solitary structures, *Geophys. Res. Lett.*, *25*, 2041–2044, doi:10.1029/98GL00636.
- Ergun, R. E., C. W. Carlson, J. P. McFadden, F. S. Mozer, L. Muschietti, I. Roth, and R. J. Strangeway (1998b), Debye-Scale Plasma Structures Associated with Magnetic-Field-Aligned Electric Fields, *Phys. Rev. Lett.*, *81*, 826–829, doi:10.1103/PhysRevLett.81.826.

- Farris, M. H., C. T. Russell, and M. F. Thomsen (1993), Magnetic structure of the low beta, quasi-perpendicular shock, *J. Geophys. Res.*, *98*, 15,285–+, doi:10.1029/93JA00958.
- Feldman, W. C., R. C. Anderson, S. J. Bame, S. P. Gary, J. T. Gosling, D. J. McComas, M. F. Thomsen, G. Paschmann, and M. M. Hoppe (1983), Electron velocity distributions near the earth's bow shock, *J. Geophys. Res.*, *88*, 96–110, doi:10.1029/JA088iA01p00096.
- Forslund, D., R. Morse, C. Nielson, and J. Fu (1972), Electron Cyclotron Drift Instability and Turbulence, *Phys. Fluids*, *15*, 1303–1318, doi:10.1063/1.1694082.
- Forslund, D. W., R. L. Morse, and C. W. Nielson (1970), Electron Cyclotron Drift Instability, *Phys. Rev. Lett.*, *25*, 1266–1270, doi:10.1103/PhysRevLett.25.1266.
- Fuselier, S. A., and D. A. Gurnett (1984), Short wavelength ion waves upstream of the earth's bow shock, *J. Geophys. Res.*, *89*, 91–103, doi:10.1029/JA089iA01p00091.
- Gary, S. P. (1981), Microinstabilities upstream of the earth's bow shock - A brief review, *J. Geophys. Res.*, *86*, 4331–4336, doi:10.1029/JA086iA06p04331.
- Greenstadt, E. W., and M. M. Mellott (1987), Plasma wave evidence for reflected ions in front of subcritical shocks - ISEE 1 and 2 observations, *J. Geophys. Res.*, *92*, 4730–4734, doi:10.1029/JA092iA05p04730.
- Hoppe, M. M., and C. T. Russell (1983), Plasma rest frame frequencies and polarizations of the low-frequency upstream waves - ISEE 1 and 2 observations, *J. Geophys. Res.*, *88*, 2021–2027, doi:10.1029/JA088iA03p02021.
- Hoppe, M. M., C. T. Russell, L. A. Frank, T. E. Eastman, and E. W. Greenstadt (1981), Upstream hydromagnetic waves and their association with backstreaming ion populations - ISEE 1 and 2 observations, *J. Geophys. Res.*, *86*, 4471–4492, doi:10.1029/JA086iA06p04471.
- Hoppe, M. M., C. T. Russell, T. E. Eastman, and L. A. Frank (1982), Characteristics of the ULF waves associated with upstream ion beams, *J. Geophys. Res.*, *87*, 643–650, doi:10.1029/JA087iA02p00643.
- Hubbard, R. F., and T. J. Birmingham (1978), Electrostatic emissions between electron gyroharmonics in the outer magnetosphere, *J. Geophys. Res.*, *83*, 4837–4850, doi:10.1029/JA083iA10p04837.
- Hull, A. J., D. E. Larson, M. Wilber, J. D. Scudder, F. S. Mozer, C. T. Russell, and S. D. Bale (2006), Large-amplitude electrostatic waves associated with magnetic ramp substructure at Earth's bow shock, *Geophys. Res. Lett.*, *33*, 15,104–+, doi:10.1029/2005GL025564.
- Kasper, J. C. (2007), Interplanetary Shock Database, harvard-Smithsonian Center for Astrophysics, Online: <http://www.cfa.harvard.edu/shocks/>.
- Kellogg, P. J. (1962), Flow of Plasma around the Earth, *J. Geophys. Res.*, *67*, 3805–+, doi:10.1029/JZ067i010p03805.
- Kennel, C. F. (1987), Critical Mach numbers in classical magnetohydrodynamics, *J. Geophys. Res.*, *92*, 13,427–13,437, doi:10.1029/JA092iA12p13427.
- Kennel, C. F., J. P. Edmiston, and T. Hada (1985), A quarter century of collisionless shock research, *Washington DC American Geophysical Union Geophysical Monograph Series*, *34*, 1–36.
- Kumar, A., and V. K. Tripathi (2006), Bernstein mode coupling to cyclotron harmonic radiation in a plasma, *Phys. Plasmas*, *13*, 052,302–+, doi:10.1063/1.2179007.
- Lampe, M., W. M. Manheimer, J. B. McBride, J. H. Orens, K. Papadopoulos, R. Shanny, and R. N. Sudan (1972), Theory and Simulation of the Beam Cyclotron Instability, *Phys. Fluids*, *15*, 662–675, doi:10.1063/1.1693961.
- Lepping, R. P., et al. (1995), The Wind Magnetic Field Investigation, *Space Science Reviews*, *71*, 207–229, doi:10.1007/BF00751330.
- Lin, R. P., et al. (1995), A Three-Dimensional Plasma and Energetic Particle Investigation for the Wind Spacecraft, *Space Science Reviews*, *71*, 125–153, doi:10.1007/BF00751328.
- Lu, Q. M., B. Lembege, J. B. Tao, and S. Wang (2008), Perpendicular electric field in two-dimensional electron phase-holes: A parameter study, *J. Geophys. Res.*, *113*, 11,219–+, doi:10.1029/2008JA013693.
- Matsukiyo, S., and M. Scholer (2006a), On microinstabilities in the foot of high Mach number perpendicular shocks, *J. Geophys. Res.*, *111*, 6104–+, doi:10.1029/2005JA011409.
- Matsukiyo, S., and M. Scholer (2006b), On reformation of quasi-perpendicular collisionless shocks, *Adv. Space Res.*, *38*, 57–63, doi:10.1016/j.asr.2004.08.012.
- Matsumoto, H., and H. Usui (1997), Intense bursts of electron cyclotron harmonic waves near the dayside magnetopause observed by GEOTAIL, *Geophys. Res. Lett.*, *24*, 49–52, doi:10.1029/96GL03650.
- Mellott, M. M., and E. W. Greenstadt (1984), The structure of oblique subcritical bow shocks - ISEE 1 and 2 observations, *J. Geophys. Res.*, *89*, 2151–2161, doi:10.1029/JA089iA04p02151.
- Muschietti, L., and B. Lembège (2006), Electron cyclotron microinstability in the foot of a perpendicular shock: A self-consistent PIC simulation, *Adv. Space Res.*, *37*, 483–493, doi:10.1016/j.asr.2005.03.077.
- Omidi, N., and D. Winske (1990), Steepening of kinetic magnetosonic waves into shocklets - Simulations and consequences for planetary shocks and comets, *J. Geophys. Res.*, *95*, 2281–2300, doi:10.1029/JA095iA03p02281.
- Paschmann, G., N. Scopke, I. Papamastorakis, J. R. Asbridge, S. J. Bame, and J. T. Gosling (1981), Characteristics of reflected and diffuse ions upstream from the earth's bow shock, *J. Geophys. Res.*, *86*, 4355–4364, doi:10.1029/JA086iA06p04355.
- Sanderson, T. R., R. Reinhard, P. van Nes, K.-P. Wenzel, E. J. Smith, and B. T. Tsurutani (1985), Observations of 35–10 1600-keV protons and low-frequency waves upstream of interplanetary shocks, *J. Geophys. Res.*, *90*, 3973–3980, doi:10.1029/JA090iA05p03973.
- Scopke, N., G. Paschmann, S. J. Bame, J. T. Gosling, and C. T. Russell (1983), Evolution of ion distributions across the nearly perpendicular bow shock - Specularly and non-specularly reflected-gyrating ions, *J. Geophys. Res.*, *88*, 6121–6136, doi:10.1029/JA088iA08p06121.
- Scudder, J. D., A. Mangeney, C. Lacombe, C. C. Harvey, and C. S. Wu (1986), The resolved layer of a collisionless, high beta, supercritical, quasi-perpendicular shock wave. III - Vlasov electrodynamics, *J. Geophys. Res.*, *91*, 11,075–11,097, doi:10.1029/JA091iA10p11075.
- Thomsen, M. F., J. T. Gosling, S. J. Bame, and M. M. Mellott (1985), Ion and electron heating at collisionless shocks near the critical Mach number, *J. Geophys. Res.*, *90*, 137–148, doi:10.1029/JA090iA01p00137.
- Thomsen, M. F., J. A. Stansberry, S. J. Bame, J. T. Gosling, and M. M. Mellott (1987), Strong electron heating at the earth's bow shock, *J. Geophys. Res.*, *92*, 10,119–10,124, doi:10.1029/JA092iA09p10119.
- Torrence, C., and G. P. Compo (1998a), Wavelet Analysis Software, atmospheric and Oceanic Sciences, University of Colorado, Online: <http://paos.colorado.edu/research/wavelets/>.
- Torrence, C., and G. P. Compo (1998b), A Practical Guide to Wavelet Analysis., *Bull. Amer. Meteor. Soc.*, *79*, 61–78, doi:10.1175/1520-0477(1998)079.
- Usui, H., W. R. Paterson, H. Matsumoto, L. A. Frank, M. Nakamura, H. Matsui, T. Yamamoto, O. Nishimura, and J. Koizumi (1999), Geotail electron observations in association with intense bursts of electron cyclotron harmonic waves in the dayside magnetosphere, *J. Geophys. Res.*, *104*, 4477–4484, doi:10.1029/1998JA900151.
- Walker, S., H. Alleyne, M. Balikhin, M. André, and T. Horbury (2004), Electric field scales at quasi-perpendicular shocks, *Ann. Geophys.*, *22*, 2291–2300.
- Williams, J. D., L.-J. Chen, W. S. Kurth, D. A. Gurnett, M. K. Dougherty, and A. M. Rymer (2005), Electrostatic solitary structures associated with the November 10, 2003, interplanetary shock at 8.7 AU, *Geophys. Res. Lett.*, *32*, 17,103–+, doi:10.1029/2005GL023079.
- Wilson III, L. B., C. A. Cattell, P. J. Kellogg, K. Goetz, K. Kersten, L. Hanson, R. MacGregor, and J. C. Kasper (2007), Waves in Interplanetary Shocks: A Wind/WAVES Study, *Phys. Rev. Lett.*, *99*, 041,101–+, doi:10.1103/PhysRevLett.99.041101.
- Wilson III, L. B., C. A. Cattell, P. J. Kellogg, K. Goetz, K. Kersten, J. C. Kasper, A. Szabo, and K. Meziane (2009), Low-frequency whistler waves and shocklets observed at quasi-perpendicular interplanetary shocks, *J. Geophys. Res.*, *114*, 10,106–+, doi:10.1029/2009JA014376.
- Wu, C. S., et al. (1984), Microinstabilities associated with a high Mach number, perpendicular bow shock, *Space Sci. Rev.*, *37*, 63–109, doi:10.1007/BF00213958.

Wygant, J. R., M. Bensadoun, and F. S. Mozer (1987), Electric field measurements at subcritical, oblique bow shock crossings, *J. Geophys. Res.*, *92*, 11,109–11,121, doi: 10.1029/JA092iA10p11109.

L.B. Wilson III, Department of Physics and Astronomy, University of Minnesota, 116 Church St SE, Minneapolis, MN 55455, USA. (wilson@physics.umn.edu)

C.A. Cattell, Department of Physics and Astronomy, University of Minnesota, 116 Church St SE, Minneapolis, MN 55455, USA. (cattell@fields.space.umn.edu)

P.J. Kellogg, Department of Physics and Astronomy, University of Minnesota, 116 Church St SE, Minneapolis, MN 55455, USA. (pauljkelllogg@gmail.com)

K. Goetz, Department of Physics and Astronomy, University

of Minnesota, 116 Church St SE, Minneapolis, MN 55455, USA. (goetz@waves.space.umn.edu)

K. Kersten, Department of Physics and Astronomy, University of Minnesota, 116 Church St SE, Minneapolis, MN 55455, USA. (kkersten@physics.umn.edu)

J.C. Kasper, Harvard-Smithsonian Center for Astrophysics, Perkins 138; MS 58, 60 Garden Street, Cambridge, MA 02138, USA. (jkasper@cfa.harvard.edu)

A. Szabo, NASA Goddard Space Flight Center, Greenbelt, MD 20771, Building 21, Room 156, USA. (adam.szabo-1@nasa.gov)

M. Wilber, University of California, Berkeley, Space Sciences Laboratory, 7 Gauss Way #7450, Berkeley, CA 94720-7450, USA. (wilber@ssl.berkeley.edu)

Table 1. Wind 3DP ELB stats across the 04/06/2000 IP shock

Species	ΔT_{es}	$\Delta T_{\perp s}$	$\Delta T_{\parallel s}$	$\Delta(T_{\perp}/T_{\parallel})_s$
Eesa Low Burst (Core/Halo)				
Core	150%	174%	110%	30%
Halo	42%	67%	5%	58%
Eesa Low Burst (Entire Distribution)				
Entire	137%	164%	96%	35%
Temperature Anisotropies $(T_{\perp}/T_{\parallel})_s$				
	16:32:03	16:32:06	16:32:09	16:32:12
Core	0.81	0.75	0.73	1.06
Halo	0.77	0.87	0.97	1.23
Entire	0.79	0.75	0.73	1.06
Global Changes Across Shock				
		$(T_2/T_1)_s$	$(T_{\perp 2}/T_{\perp 1})_s$	$(T_{\parallel 2}/T_{\parallel 1})_s$
Core		3.3	3.8	2.5
Halo		1.4	1.8	0.8
Entire		3.0	3.7	2.3

Table 2. Wind 3DP Global ELB stats across the five IP shocks

Species	ΔT_{es}	$\Delta T_{\perp s}$	$\Delta T_{\parallel s}$	ΔB	α	α_{\perp}
1996-04-03 Event						
Core	45%	46%	45%		0.15	0.15
Halo	134%	125%	153%		1.03	0.95
Entire	-14%	-15%	-13%	57%	-0.45	-0.45
1996-04-08 Event						
Core	54%	48%	65%		0.12	0.07
Halo	119%	108%	144%		0.78	0.66
Entire	-15%	-19%	-6%	62%	-0.56	-0.60
1997-10-24 Event						
Core	54%	57%	49%		-0.28	-0.26
Halo	87%	103%	60%		0.04	0.20
Entire	4%	10%	-8%	92%	-0.79	-0.72
1997-12-10 Event						
Core	12%	13%	9%		-0.72	-0.71
Halo	44%	38%	55%		-0.40	-0.46
Entire	5%	6%	2%	121%	-0.79	-0.78
2000-04-06 Event						
Core	228%	281%	153%		0.83	1.36
Halo	37%	84%	-23%		-1.08	-0.61
Entire	209%	267%	128%	266%	0.63	1.22

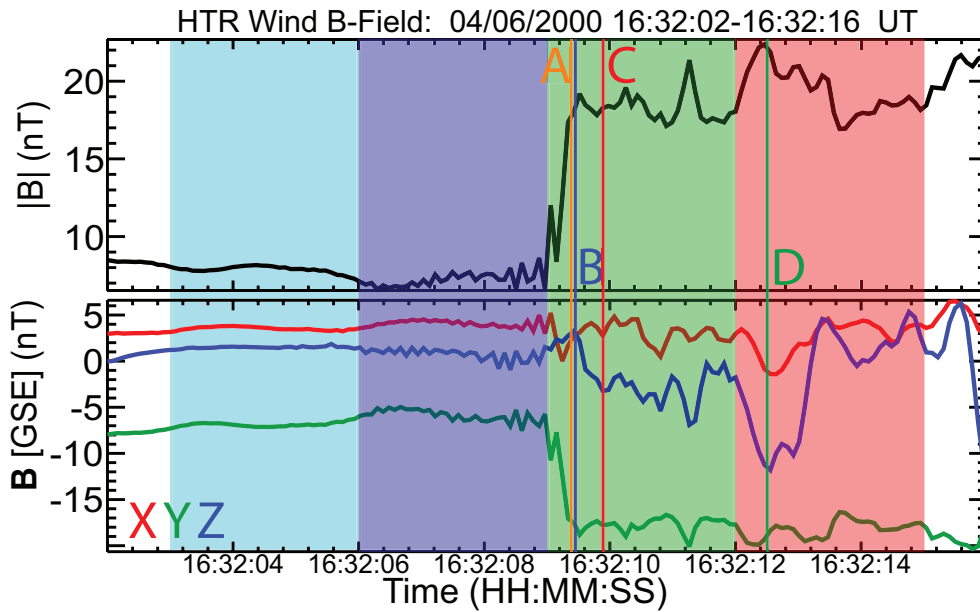


Figure 1. The plot shows the magnitude and the GSE coordinates of the magnetic field for the IP shock on 04/06/2000. The shaded regions correspond to the time ranges of each particle distribution found in Figure 2. The vertical color-coded lines indicate the locations of the TDS samples shown in Figure 3 labeled with the respective capital letters. The time range of the plot is 16:32:02-16:32:16 UT and the shock arrival time is 16:32:09.2 UT.

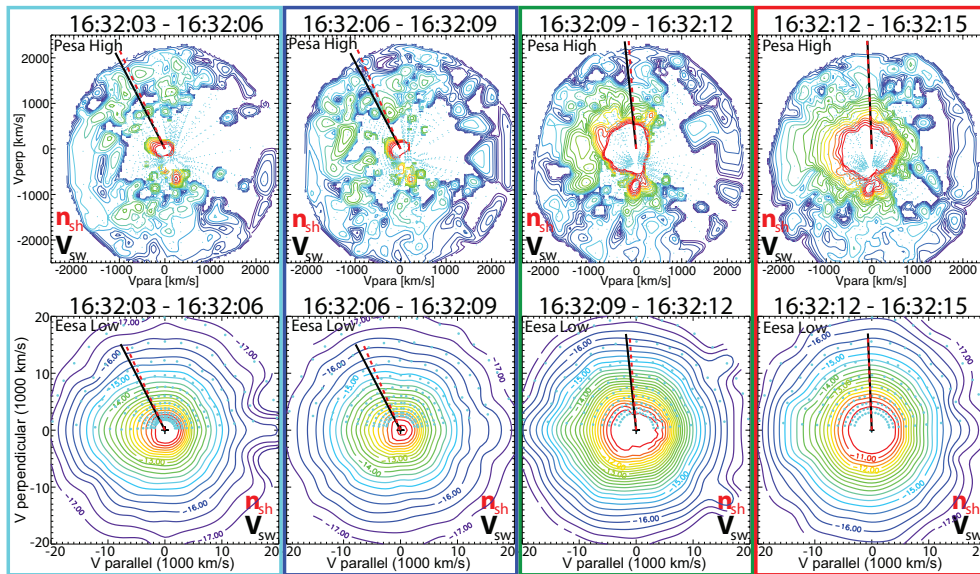


Figure 2. Four particle distributions from both the PHB (top row) and ELB (bottom row) detectors on the Wind 3DP instrument. The horizontal axis of each plot is parallel to the magnetic field and the vertical axis is perpendicular in the plane created by the solar wind velocity and magnetic field direction. Each pair of samples, ELB and PHB, are outlined by a colored box which corresponds to the shaded regions in Figure 1. The black solid line represents the projection of the solar wind velocity and the red dotted line represents the shock normal vector projection. Note the sample times are the same for each instrument.

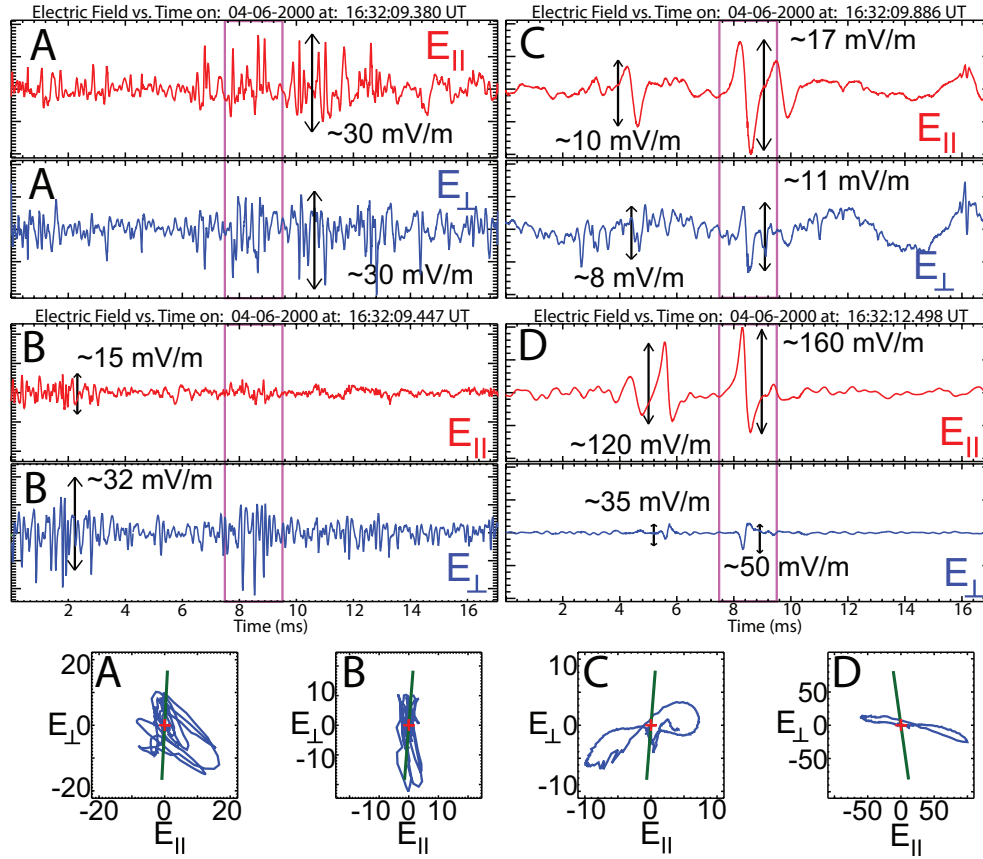


Figure 3. Four waveform captures in and around the ramp region of the 04/06/2000 IP shock. The waves in Panels **A** (16:32:09.380 UT) and **B** (16:32:09.447 UT) are trains of steepened waves while the waves in Panels **C** (16:32:09.886 UT) and **D** (16:32:12.498 UT) are solitary-like waves. The top panels of each waveform (red) corresponds to E_{\parallel} and the bottom (blue) corresponds to E_{\perp} . Their respective peak-to-peak amplitudes are marked by the vertical black arrows. Below the four waveforms are their respective hodograms labeled with the same capital letters corresponding to the time range defined by the magenta boxes in each TDS sample. The solid green line in each hodograms represents the XY-projection of the shock normal vector in FACs.

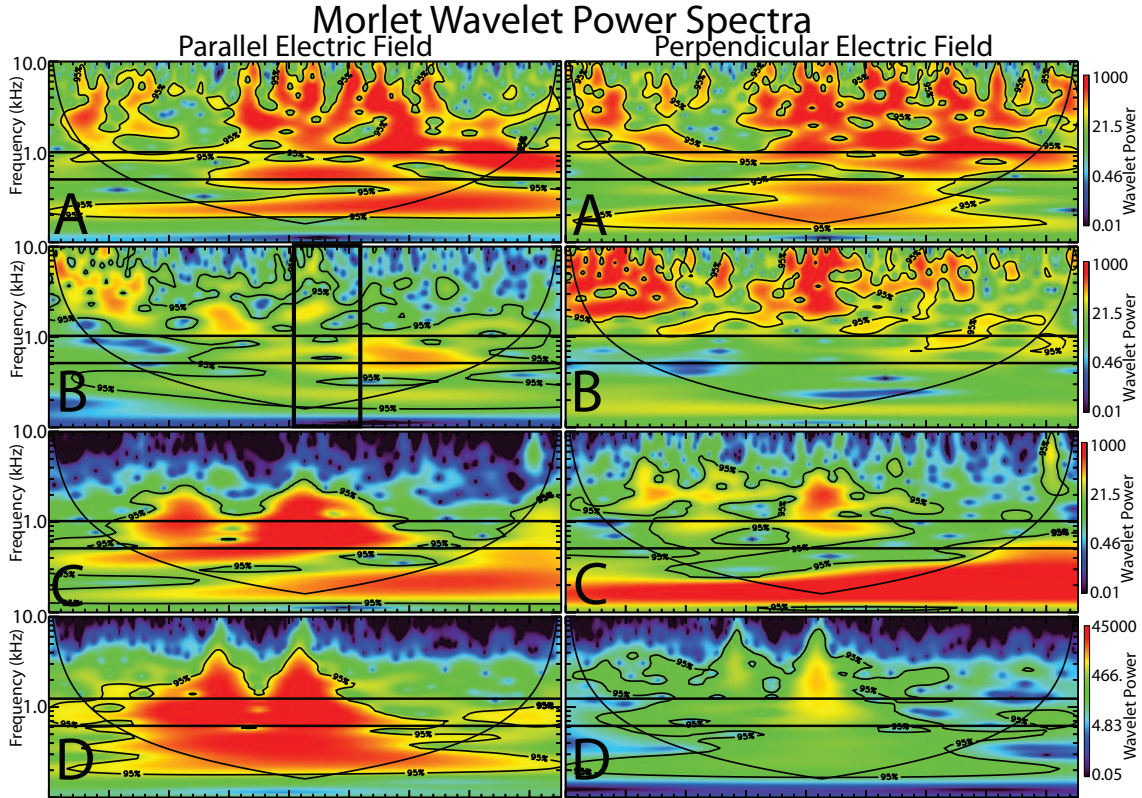


Figure 4. The Morlet wavelet power spectrum for the four waveforms in Figure 3, labeled **A** through **D** accordingly. The left column is for E_{\parallel} and the right for E_{\perp} . The top three rows share the same spectral range of 0.01 to 1000 for the wavelets while waveform **D** ranged from 0.05 to 45000, while all four have been normalized to conserve energy in the wavelet transformations. In each panel, two horizontal lines mark the fundamental and first harmonic of the electron cyclotron frequency. The bowl-like line plotted in each spectra marks the cone of influence while the contours mark the 95% confidence levels [Torrence and Compo, 1998b].

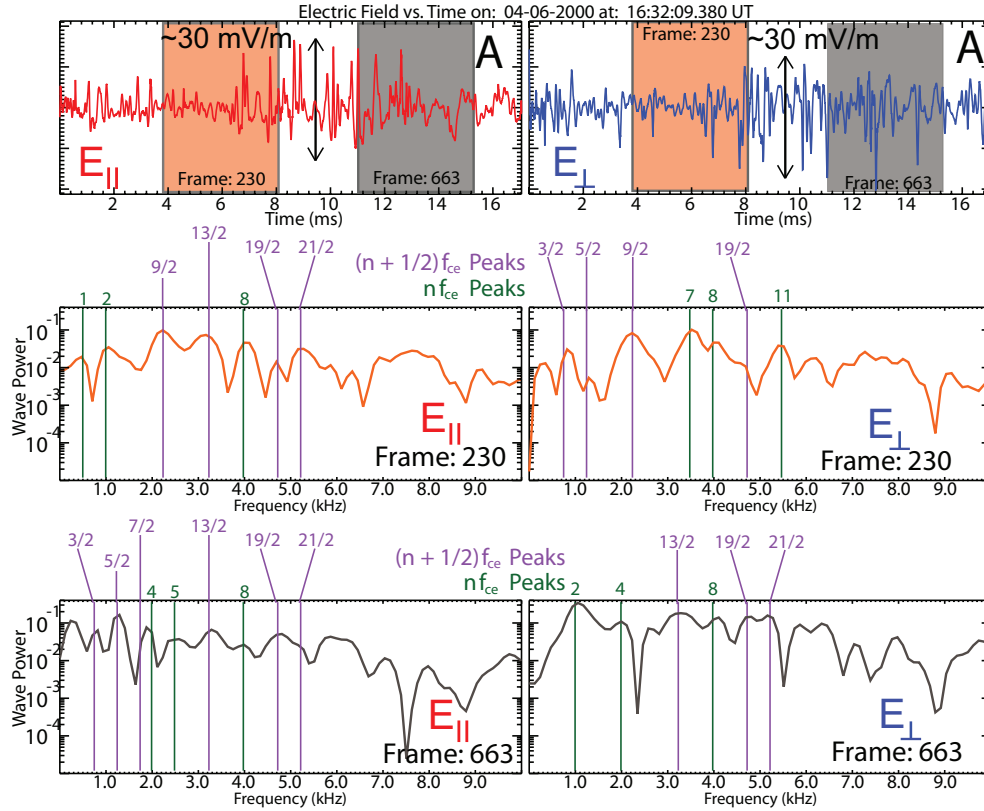


Figure 5. Example snapshots of windowed FFTs of waveform **A** from Figure 3. The left-hand column of panels shows E_{\parallel} , the power spectra ($\text{mV}/\text{m}^2/\text{Hz}$) versus frequency (kHz) for the orange box, and the power spectra versus frequency for the black box, respectively. The right-hand column shows the same for E_{\perp} . The vertical lines in the power spectra correspond to integer (green) and half-integer (purple) multiples of the electron cyclotron frequency. All power spectra plots in this figure range from 10^{-5} to 4×10^{-1} .

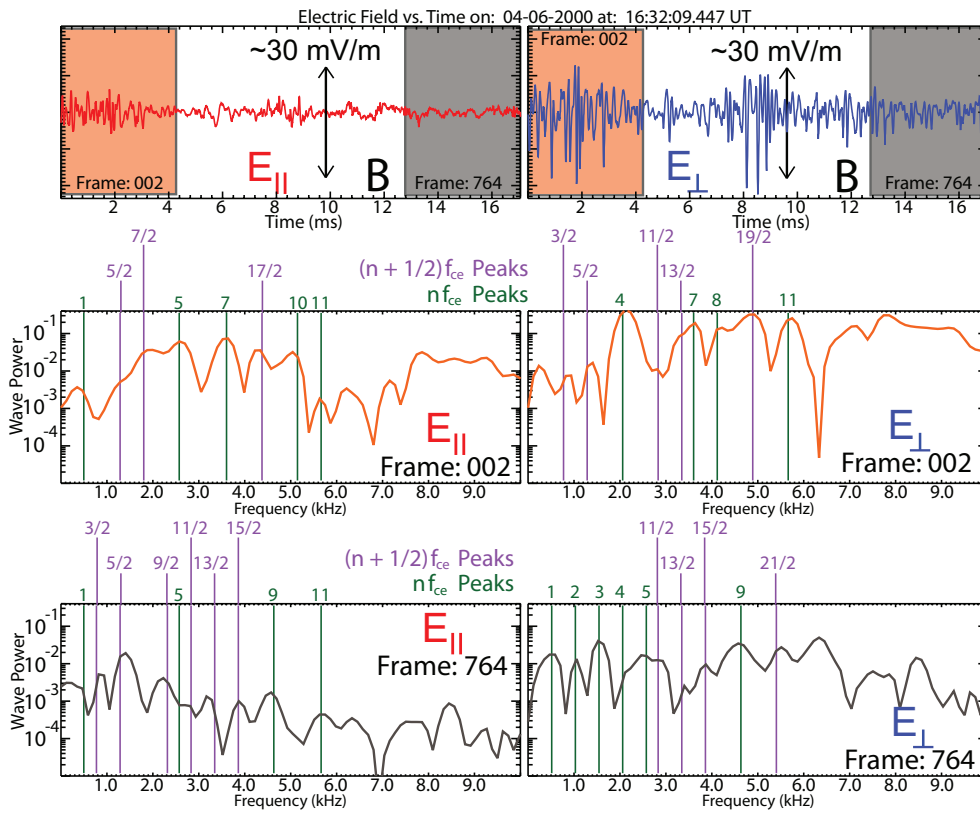


Figure 6. Example snapshots of windowed FFTs of waveform **B** from Figure 3. The format is the same as Figure 5. All power spectra plots in this figure range from 10^{-5} to 4×10^{-1} .

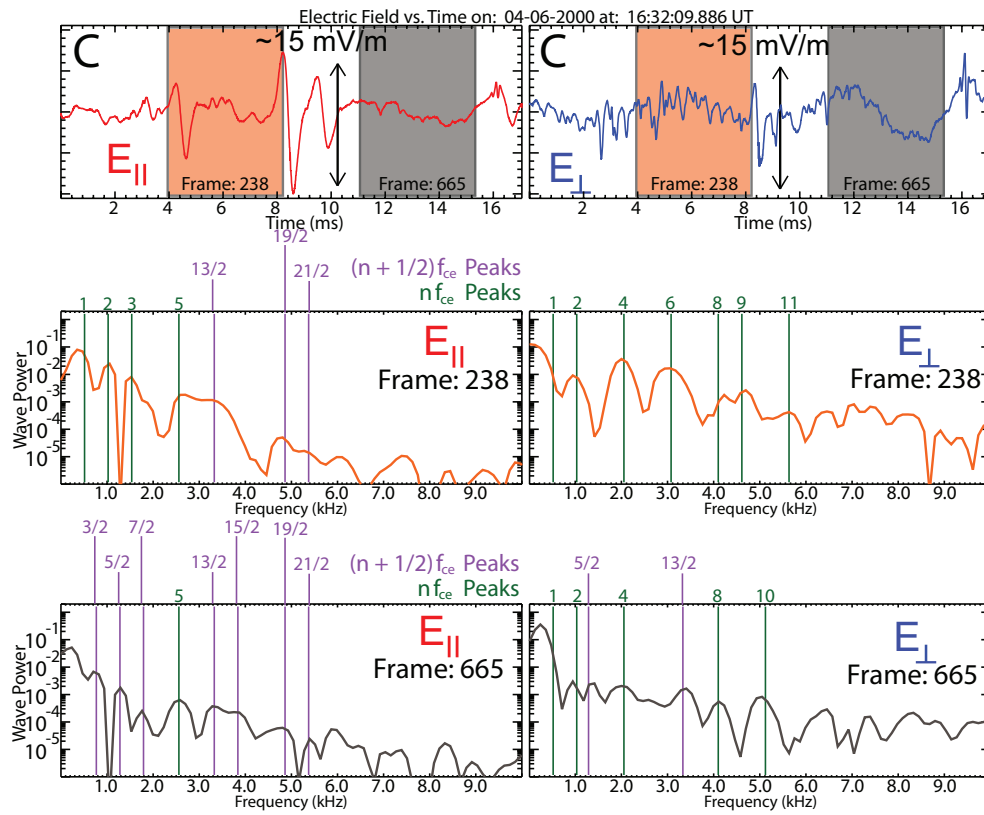


Figure 7. Example snapshots of windowed FFTs of waveform **C** from Figure 3. The format is the same as Figure 5. All power spectra plots in this figure range from 10^{-6} to 2×10^0 .

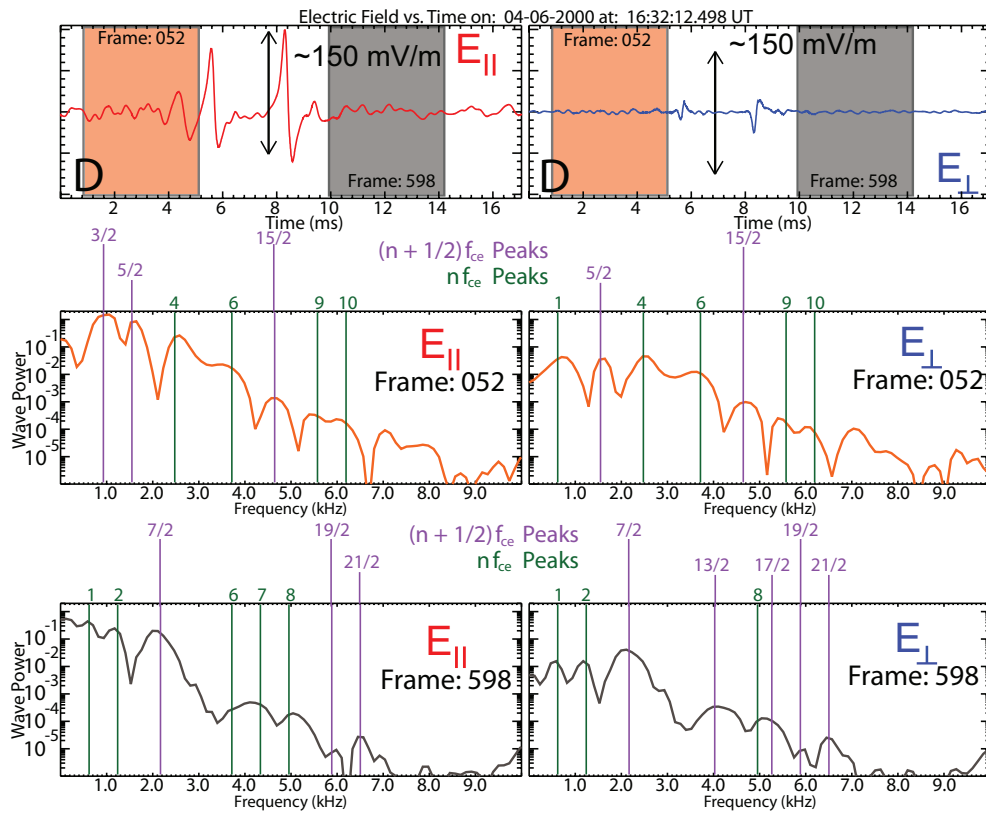


Figure 8. Example snapshots of windowed FFTs of waveform **D** from Figure 3. The format is the same as Figure 5. All power spectra plots in this figure range from 10^{-6} to 2×10^0 .

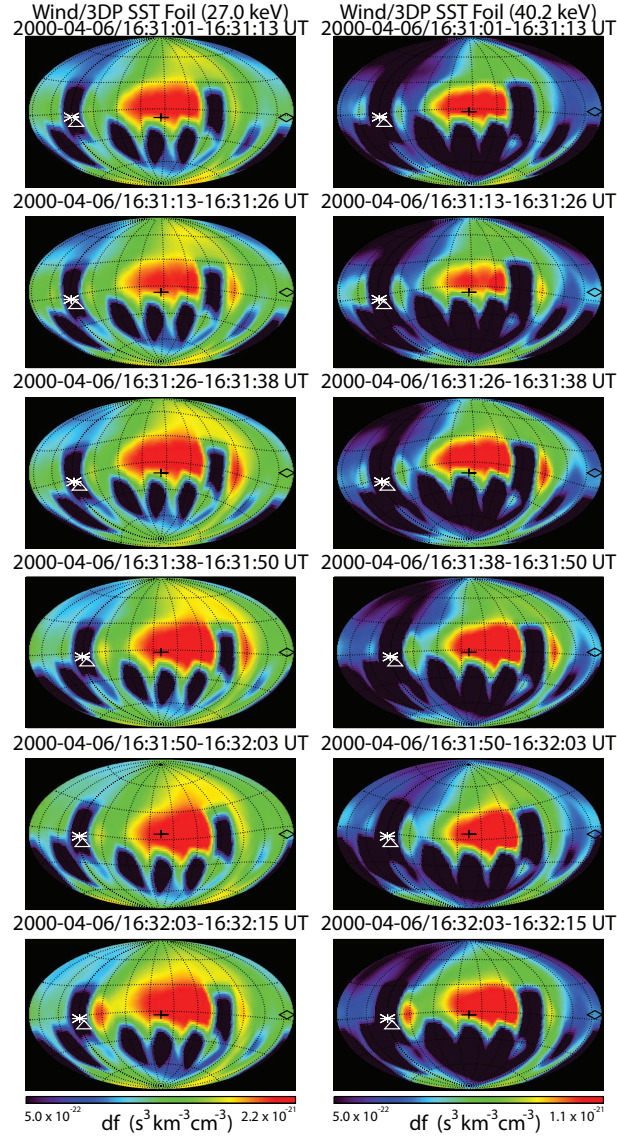


Figure 9. Hammer-Aitoff projections of SST Foil observations from 16:31:01 UT to 16:32:15 UT of field-aligned enhancements of 27-40 keV electrons. The + symbol represents the magnetic field-aligned direction, diamond the anti-parallel field direction, asterisks is the solar wind direction, and the triangle represents the shock normal direction. The left column plots the 27 keV energy bin while the right plots the 40 keV energy bin. All images in each column have the same color scales, shown at the bottom of each column.

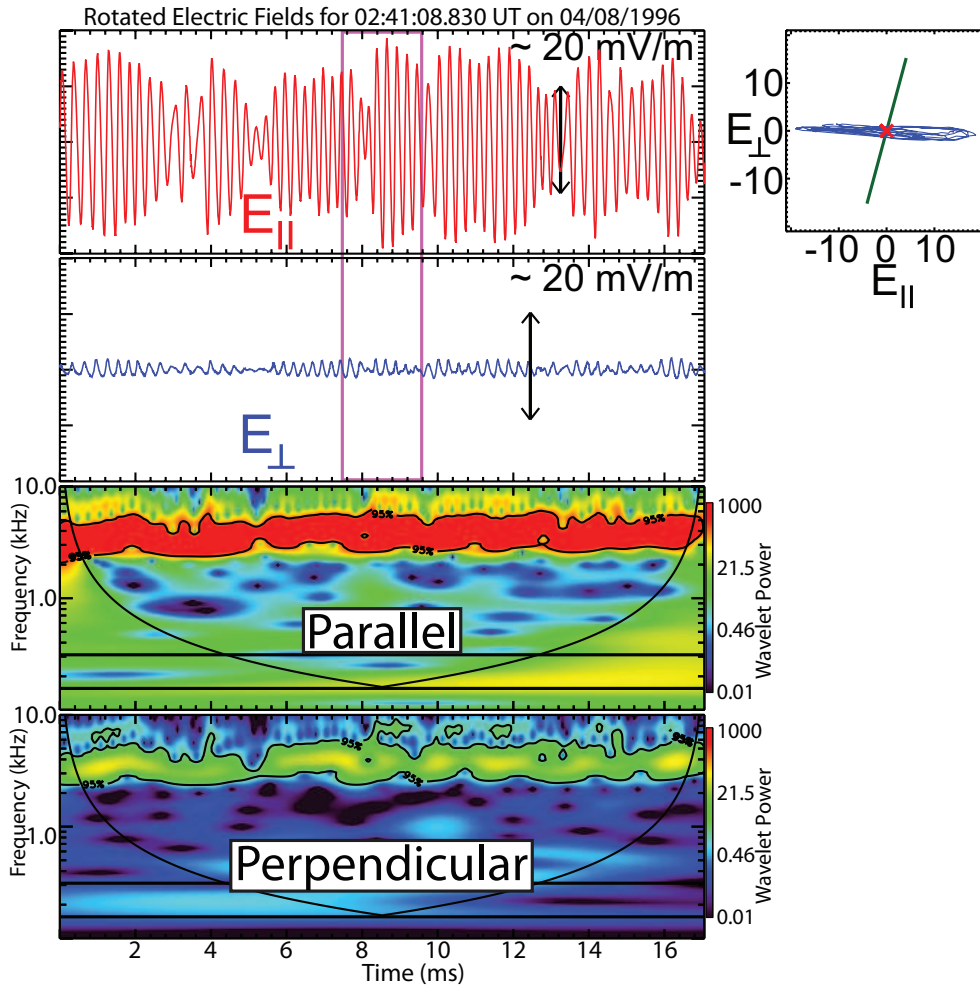


Figure 10. An example IAW observed in the shock ramp of the 04/08/1996 event of *Wilson III et al.* [2009]. The format is similar to that of Figures 3 and 4, except that only one waveform is shown and the wavelets are in the same plot. The parallel and perpendicular component wavelet transforms are labeled respectively. The solid green line in the hodogram on the right represents the XY-projection of the shock normal vector in FACS.